Research Article

Journal of Environmental Nanotechnology

Green and Chemically Synthesized Silver Nanoparticle-Reinforced Coconut Coir Dust/Water-borne Polyurethane Biocomposites for Lightweight Antibacterial Applications

Sobini X Pushpa[1], G. Senthilkumar[2], Senthilkumar Pachiyappan[3], N. Viswanathan[4], J. Kumaresan[5] and R. Girimurugan[6]*

[1]Department of Computer Science and Engineering, St. Xavier's Catholic College of Engineering, Nagercoil, TN, India
[2]Department of Mechanical Engineering, Bannari Amman Institute of Technology, Sathyamangalam, TN, India
[3]Department of Chemical Engineering, Saveetha Engineering College, Chennai, TN, India
[4]Department of Mechanical Engineering, Nandha College of Technology, Perundurai, TN, India
[5]Department of Electrical & Electronics Engineering, Nandha College of Technology, Perundurai, TN, India
[6]Department of Mechanical Engineering, Nandha College of Technology, Perundurai, TN, India
Received: 20.06.2026 Accepted: 21.07.2026 Published: xx.xx.xxxx
*girinctmech@gmail.com

ABSTRACT

The present investigation explores a sustainable strategy for utilizing coconut coir dust, a largely underexploited by-product generated from agricultural waste, for the development of lightweight materials. Rather than employing this lignocellulosic waste in conventional low-value applications, the study incorporates environmentally synthesized silver nanoparticles (Ag NPs) into a coconut coir dust-reinforced water-borne polyurethane (WPU) matrix to fabricate functional biocomposites. The optimum formulation was identified using an integrated MEREC–RAFSI multi-criteria decision-making approach. Silver nanoparticles were produced through both chemical reduction and green synthesis routes utilizing lemon peel extract as a stabilizing and reducing agent. Structural, morphological, thermal, and antibacterial characteristics of the developed composites were systematically evaluated using XRD, FTIR, FESEM, thermogravimetric analysis (TGA), UV–Visible spectroscopy, and dynamic light scattering (DLS). The results confirmed the successful formation and homogeneous dispersion of Ag nanoparticles throughout the polymer matrix. DLS analysis revealed average particle sizes of approximately 55 nm and 61 nm for chemically synthesized and green-synthesized Ag nanoparticles, respectively, while XRD analysis indicated crystallite sizes of 21.0 and 20.84 nm. Mechanical evaluation demonstrated notable improvements in performance, with tensile strength values ranging from 22.4 ± 1.0 to 26.4 ± 0.4 MPa, tensile modulus from 31.2 ± 1.1 to 42.2 ± 0.4 MPa, and excellent flexing durability exceeding 8400 cycles, confirming suitability for lightweight applications. Furthermore, antibacterial assessment indicated strong inhibitory activity against both *Bacillus subtilis* and *Escherichia coli*, with the G4 composite exhibiting inhibition zones of 15.3 mm and 14.2 mm, respectively. The developed biocomposite therefore represents a promising eco-friendly alternative to conventional materials, combining waste valorization, enhanced mechanical integrity, thermal stability, and effective antibacterial functionality.

Keywords: Antibacterial activity; Green synthesis; Silver nanoparticles; Optimization; Mechanical properties.

1. INTRODUCTION

The growing demand for sustainable and functional materials has encouraged the utilization of lignocellulosic waste resources as reinforcements in polymer composites (Subbarao *et al.* 2026). Lemon peel extract contains phenolic, flavonoid, and other phytochemical constituents capable of participating in Ag^+ reduction and subsequent nanoparticle surface stabilization. Therefore, lemon peel extract was selected specifically as the reducing and capping medium for green AgNP synthesis rather than as a direct composite additive (Ertekin, 2025). Among these materials, coconut coir dust has gained increasing attention due to its abundance, biodegradability, low cost, and potential for value-added applications (Gupta *et al.* 2026). Furthermore, the incorporation of silver nanoparticles into environmentally friendly water-borne polyurethane matrices offers an effective approach for developing composite materials with enhanced antibacterial, mechanical, and thermal performance (Krishnasamy *et al.* 2026). Both synthesis routes were investigated to provide a controlled comparison between $NaBH_4$-based chemical reduction and phytochemical-mediated green synthesis. Chemical synthesis offers controlled reduction conditions, whereas lemon-peel-assisted synthesis reduces dependence on conventional reducing chemicals and enables evaluation of whether the greener route can

provide comparable structural, mechanical, and antibacterial performance.

Previous studies demonstrate that natural lignocellulosic reinforcements can improve the mechanical and thermal performance of polymer composites, while AgNP incorporation can additionally provide antibacterial activity, moisture resistance, and structural reinforcement. Coir-based polyurethane systems have shown promising interfacial and mechanical characteristics (Camillo *et al.* 2023), whereas AgNP-containing biodegradable composites have exhibited improved tensile, thermal, and antibacterial properties (Balasubramanian *et al.* 2026; Blessymol et al, 2023; Sivaranjani et al. 2025); (Meniche *et al.* 2026). Collectively, previous studies show that coir reinforcement primarily improves structural performance, whereas AgNP incorporation introduces antibacterial and additional barrier functionality. However, most studies emphasize either reinforcement or nanoparticle functionality independently, providing limited understanding of their combined effects in WPU-based lightweight composites (Pereira *et al.* 2025). However, these approaches have generally investigated natural reinforcement, AgNP functionality, or polymer optimization separately, leaving limited information on their combined performance in water-borne polyurethane systems. Conventional PU and TPU insole materials provide flexibility, cushioning, and durability, but their performance depends strongly on hardness and repeated-flexing resistance. Reported TPU orthoses span approximately Shore A 60–90, with excessively low or high hardness adversely affecting perceived support or flexibility. Accordingly, the present study considers tensile behavior, Shore A hardness, tear resistance, flexing endurance, moisture response, and antibacterial performance collectively rather than assessing mechanical strength alone.

A green synthesis approach utilizing lemon peel extract was employed to produce $ZnFe_2O_4$ nanoparticles for incorporation into chitosan films, wherein the addition of nanoparticles improved tensile strength, barrier performance, and overall material stability, highlighting the potential of plant-derived additives in biodegradable polymer systems (Hassan *et al.* 2024). Similarly, bio-based rigid polyurethane foam reinforced with silica nanoparticles derived from agricultural waste demonstrated improved mechanical and thermal performance, with enhanced nanoparticle dispersion and superior thermal stability confirmed through advanced characterization (Osorio *et al.* 2025). The integration of natural fiber reinforcements into a biodegradable polymer matrix has also gained considerable attention as a strategy to improve the structural and functional properties of green composites. Polyester composites reinforced with banana fibers and coconut shell filler exhibited improved tensile and flexural strength at optimum filler loading (Kannan and Thangaraju, 2023), while biodegradable thermoplastic cassava starch composites reinforced with coconut husk fibers of varying particle sizes demonstrated enhanced thermal stability and significant mechanical improvements, particularly for smaller fiber sizes (Jumaidin *et al.* 2024). The optimization of alkali treatment parameters on coir fibers using ANOVA and response surface methodology further revealed substantial enhancements in tensile strength, elastic modulus, crystallinity, and thermal stability (Ru *et al.* 2022). A novel coconut tree secondary flower leaf stalk (CSF) fiber subjected to benzoylation treatment demonstrated improved crystallinity, surface morphology, and thermal stability, with tensile strength reaching 650.54 MPa and Young's modulus of 1.89 GPa (Ramkumar *et al.* 2022).

Silver nanoparticles (AgNPs) synthesized via plant-assisted green routes have attracted particular attention owing to their multifunctional biomedical and antimicrobial properties. Both chemical and plant-assisted synthesis approaches have been employed for the preparation of AgNPs for antibacterial applications, demonstrating effective inhibition of *E. coli* and *P. aeruginosa* (Guerrero *et al.* 2026). Plant-assisted synthesis of AgNPs from *Calotropis gigantea* leaf extract yielded nanoparticles with strong antibacterial activity, antioxidant properties, and significant inhibition against *Helicobacter pylori*, demonstrating their multifunctional biomedical potential (Kamalesan *et al.* 2026). Similarly, green-synthesized AgNPs from *Prunus africana* exhibited notable antibacterial activity against multidrug-resistant bacterial strains (Lemeitaron *et al.* 2026), while bio-inspired synthesis using *Spermacoce alata* leaf extract produced stable and crystalline nanoparticles with strong antibacterial, antibiofilm, and antioxidant activities (Debnath *et al.* 2026).

Plant-assisted AgNP studies consistently demonstrate that phytochemical-mediated synthesis can produce stable nanoparticles with substantial antibacterial activity, supporting their incorporation into functional polymer composites (Boncooğlu *et al.* 2026), (Kularia *et al.* 2026), while AgNPs derived from *Arbutus unedo* extracts exhibited remarkable antibacterial activity against *E. coli* and *S. aureus*, along with low cytotoxicity and enzyme inhibitory properties (Tavukcuoglu *et al.* 2026).

The incorporation of AgNPs into biodegradable polymer films and biocomposite systems has further expanded their applicability in active packaging and structural material domains. Despite these developments, limited research has simultaneously integrated coconut coir dust, WPU, and AgNPs while directly comparing chemical and plant-assisted AgNP synthesis routes. Furthermore, systematic optimization of such composites using objective multi-criteria decision-making remains insufficiently explored. Eco-friendly AgNPs incorporated into biodegradable alginate films for active

packaging exhibited improved antibacterial activity, tensile strength, thermal stability, and barrier properties, while nanobiocomposites reinforced with chemically treated natural fibers and AgNPs@PVA demonstrated enhanced tensile strength and reduced water absorption, particularly for $KMnO_4$-treated fiber composites (Arumugam *et al.* 2020).

Accordingly, this study aimed to: (i) evaluate coconut coir dust/WPU compositions containing 0–30 wt.% coir; (ii) identify the optimum coir/WPU formulation using MEREC–RAFSI; (iii) incorporate chemically and green-synthesized AgNPs at 1.25, 2.50, 3.75, and 5.00 wt.%; and (iv) compare their mechanical, physical, thermal, morphological, and antibacterial performance. It was hypothesized that AgNP incorporation would improve composite compactness, mechanical durability, moisture resistance, and antibacterial activity, while green-synthesized AgNPs would provide comparable performance to chemically synthesized AgNPs through a more environmentally favorable synthesis route. The synthesized nanoparticles were incorporated into coconut coir dust-reinforced water-borne polyurethane composites, and the resulting insole materials were evaluated for their mechanical, physical, and antibacterial performance. The utilization of coconut coir dust in a polyurethane matrix provides a sustainable solution for converting waste into value-added lightweight materials. Furthermore, MEREC–RAFSI-based multi-criteria decision-making was employed to determine the optimum composite formulation. The novelty of this study lies in integrating coconut coir dust with WPU and AgNPs synthesized through both chemical and lemon-peel-assisted green routes, followed by MEREC–RAFSI optimization to identify a mechanically balanced formulation for lightweight antibacterial applications. This strategy establishes an effective pathway for waste valorization while ensuring the development of durable and functional materials. The proposed material combines three sustainability-oriented features: valorization of coconut coir waste, use of water-borne polyurethane, and phytochemical-assisted AgNP synthesis. Water-borne polyurethane employs water rather than conventional organic solvents as the principal dispersion medium and is widely recognized for reduced VOC emissions, while coir utilization provides a value-added pathway for lignocellulosic waste.

2. MATERIALS AND METHODOLOGY

2.1 Materials

Coconut coir dust (<150 µm) was obtained locally, washed, and dried at 60 °C for 24 h. $AgNO_3$ (≥99.9%), $NaBH_4$ (≥98%), ethanol (≥99.5%), and NaOH (≥98%) were procured from Star Scientific Enterprises, Erode, India. The commercial aliphatic WPU dispersion contained 35 ± 2 wt.% solids, with a density of 1.05 g cm^{-3}, viscosity of 200 mPa·s, and pH of 7.5–8.5.

2.2 Synthesis of Silver NPs

2.2.1 Chemical Synthesis

Chemically synthesized silver nanoparticles (C-Ag) were prepared by reducing $AgNO_3$ with $NaBH_4$. $AgNO_3$ solution (100 mL, 1.0 mM) was cooled to 5 ± 2 °C in an ice bath and stirred at 600 rpm. Freshly prepared $NaBH_4$ solution (20 mL, 10 mM) was added dropwise at approximately 1 mL min^{-1}. The solution pH was adjusted to 9.0 ± 0.2 using 0.1 M NaOH. The appearance of a dark-brown suspension indicated AgNP formation. The suspension was stirred at 600 rpm for 2 h at 25 ± 2 °C and then centrifuged at 6000 rpm for 15 min. The recovered particles were washed three times with deionized water and twice with ethanol before drying at 60 °C for 12 h (C-Ag) (Dayana *et al.* 2026).

2.2.2 Plant-assisted Synthesis

Green-synthesized silver nanoparticles (G-Ag) were prepared using lemon-peel extract. Dried lemon-peel pieces (50 g) were added to 100 mL of deionized water and heated at 90 °C for 2 h under stirring at 400 rpm. After cooling, the extract was filtered twice through Whatman No. 1 filter paper. For AgNP synthesis, 50 mL of lemon-peel extract was mixed with 50 mL of 1.0 mM $AgNO_3$ solution, corresponding to an extract-to-precursor volume ratio of 1:1. Preliminary trials conducted at ratios of 1:3, 1:1, and 3:1 showed that the 1:1 ratio produced the strongest surface-plasmon-resonance band and the most stable suspension. The reaction pH was adjusted to 8.0 ± 0.2 using 0.1 M NaOH, and the mixture was stirred at 500 rpm and 60 ± 2 °C for 2 h. The resulting particles were centrifuged at 6000 rpm for 15 min, washed three times with deionized water and twice with ethanol, and dried at 60 °C for 12 h.

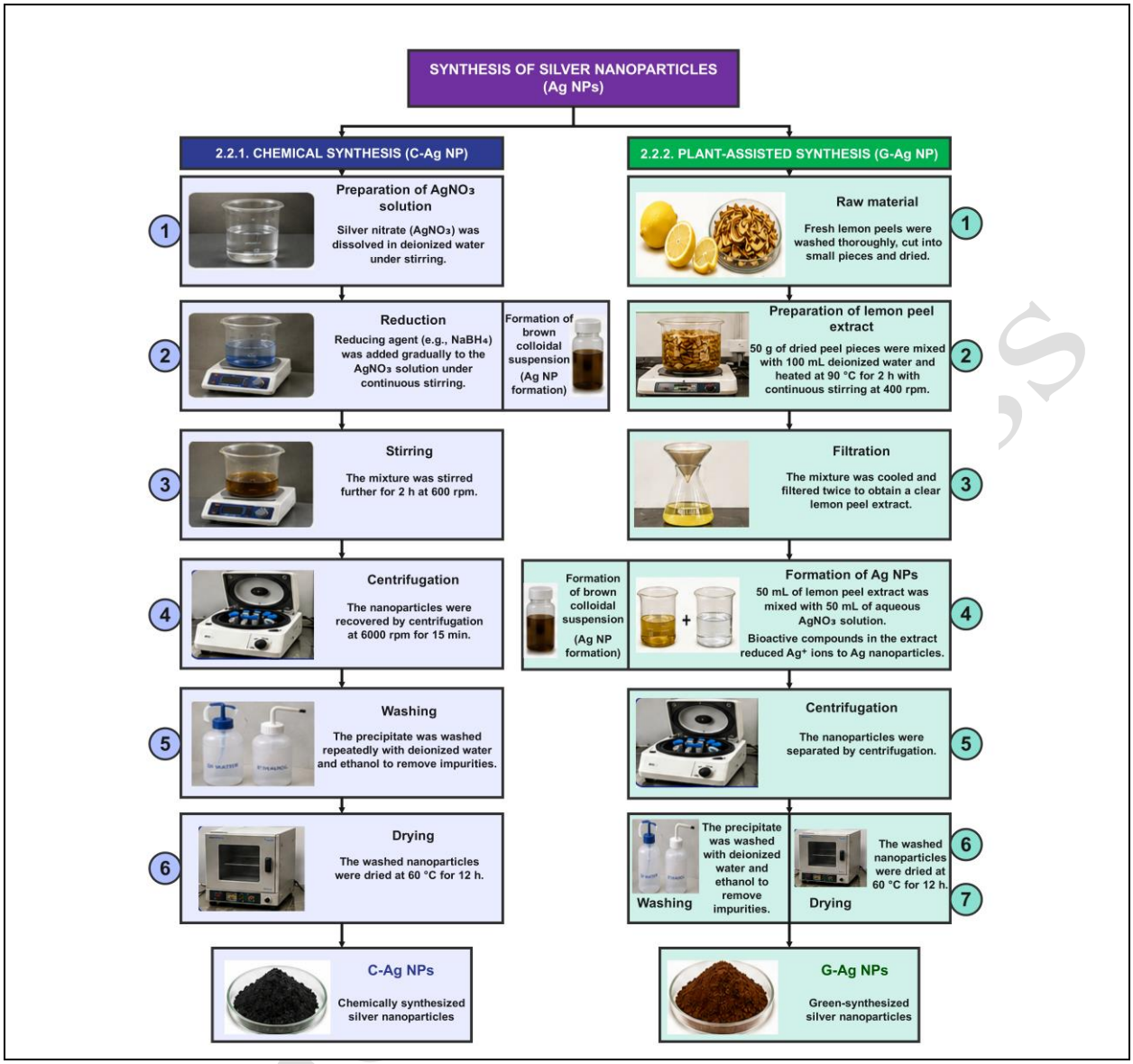

Fig. 1: Synthesis of Ag nanoparticles (C-Ag and G-Ag) via chemical and green methods

2.3 Composite Preparation

The collected coconut coir was pulverized into fine powder using a mechanical grinder and blended with water-borne polyurethane (WPU) resin at different weight fractions of 0:100 (A), 5:95 (B), 10:90 (C), 15:85 (D), 20:80 (E), 25:75 (F), and 30:70 (G) to obtain a homogeneous mixture. Higher coir loadings, such as 35:65 and 40:60, produced highly viscous mixtures that were unsuitable for casting. Coir-dust contents of 0–30 wt.% were selected to cover the workable processing range of the WPU system. Preliminary casting trials showed that loadings below 5 wt.% produced limited reinforcement, whereas loadings above 30 wt.% caused excessive viscosity, incomplete wetting, and non-uniform casting. Therefore, 5 wt.% intervals were used to determine the composition providing the most favorable balance between strength, stiffness, elongation, and processability. The prepared slurry was cast into glass molds measuring 130 × 30 × 2 mm3 and allowed to dry under ambient conditions.

2.4 Preparation of Nanoparticle-added Composites

AgNP loading was calculated on a dry-mass basis relative to the mass of coconut coir dust. For 25 g of coir dust, AgNP quantities of 0.3125, 0.6250, 0.9375, and 1.2500 g represented loadings of 1.25, 2.50, 3.75, and 5.00 wt.%, respectively. In each case, 15 mL of deionized water was used only as a temporary dispersion medium and was removed during drying; therefore, it was not included in the final composite composition. The required AgNP mass was dispersed in 15 mL of deionized water by probe ultrasonication at 20 kHz and 150 W for 15 min using a 5 s on/5 s off pulse cycle. WPU was

subsequently added and mechanically stirred at 600 rpm for 20 min, followed by gradual incorporation of coir dust and further mixing at 500 rpm for 15 min. The mixture was vacuum-degassed at −0.08 MPa for 10 min and cast into glass molds measuring 130 × 30 × 2 mm³. The composites were dried at 25 ± 2 °C and 50 ± 5% relative humidity for 72 h, post-dried at 60 °C for 6 h, and conditioned at 23 ± 2 °C and 50 ± 5% relative humidity for 48 h before testing.

2.5 Characterization Techniques

Particle size distribution of synthesized Ag nanoparticles was analyzed by Zetasizer Nano ZS particle size analyzer (Malvern Panalytical, UK) equipped with a 633 nm He–Ne laser source. Optical properties of synthesized nanoparticles were investigated by a UV–2600 UV–Visible spectrophotometer (Shimadzu, Japan) operated over the desired wavelength range at an appropriate scanning rate. Prior to analysis, the instrument was calibrated using Ag nanoparticle suspensions with concentrations of 10- 40 ppm. Absorbance spectra were subsequently recorded over the wavelength range of 200–800 nm to examine the optical response of the synthesized nanoparticles.

FTIR spectroscopy of coconut coir dust, water-borne polyurethane, Ag nanoparticles, and the fabricated biocomposites was carried out using a Spectrum Two FTIR spectrometer (PerkinElmer, USA). Spectra were collected over the wavenumber range of 4000–500 cm^{-1} to see functional groups and intermolecular interactions present within the constituent materials and composite structures.

The crystalline phase and structural characteristics of the synthesized Ag nanoparticles was analyzed by XRD-7000 X-ray diffractometer (Shimadzu, Japan). The diffraction data were collected employing Cu Kα radiation (λ =$\lambda = 1.5406$Å), operated at 30 mA and 40 kV. Crystallite size of nanoparticles was calculated from the major diffraction peaks by DebyeScherrer relation, $D = K\lambda/(\beta\cos\theta)$, here D shows crystallite size, K were Scherrer constant (0.9), λ represents X -ray wavelength, β corresponds to full width at half maximum (FWHM) seen in radians, and θ were Bragg angle (Deleanu *et al.* 2024).

The thermal stability and degradation characteristics of fabricated biocomposites were investigated using a TGA 550 thermogravimetric analyzer (TA Instruments, USA). Approximately 5–10 mg of each sample was placed in a platinum crucible and heated from ambient temperature to 700 °C in a nitrogen atmosphere with a flow rate of 20 mL/min. An empty reference pan was employed throughout the analysis to evaluate the weight-loss behavior and thermal decomposition profile of the composite specimens.

The surface characteristics of the synthesized Ag nanoparticles and fabricated biocomposites were examined using a field emission scanning electron microscope (GEMINI, ZEISS). Prior to imaging, specimens were sputter-coated with a thin platinum layer and observed at an accelerating voltage of 5.0 kV. Elemental analysis was performed by an energy-dispersive X-ray system coupled with FESEM. In addition, particle size distribution of Ag nanoparticles was estimated from the FESEM micrographs by ImageJ image analysis software.

2.6 Mechanical Testing

Tensile strength, tensile modulus, and elongation at break were measured using a universal testing machine in accordance with ASTM D412, Method A. Dumbbell specimens with an overall length of 115 mm, gauge length of 50 mm, narrow-section width of 6 mm, and thickness of 2.0 ± 0.1 mm were tested at a crosshead speed of 500 mm min^{-1}. Flexing endurance was evaluated using a flex-testing apparatus according to ASTM D2097 under a 2 kg load using specimens measuring 70 × 10 × 2 mm³. Stitch-tear resistance was measured according to ASTM D4705 using specimens measuring 50 × 25 × 2 mm³ at a crosshead speed of 100 mm min^{-1}. Shore A hardness was measured according to ASTM D2240 using a 1 kg applied load and a dwell time of 15 s. Five independently prepared specimens were tested for each formulation, and the results were expressed as mean ± standard deviation. Statistical analysis was performed using one-way analysis of variance (ANOVA), followed by Tukey's honestly significant difference post-hoc test for pairwise comparison.

2.7 Optimization with MCDM

2.7.1 Criteria Weighting by MEREC

Step 1. Construct the decision matrix and classify criteria. Build $X = \left[x_{ij}\right]_{m\times n}$ from the responses of alternatives $\mathrm{A}-\mathrm{G}$and classify each criterion as beneficial (B, larger-is-better) or non-beneficial (NB, smaller-is-better).

Step 2. Normalize the matrix (MEREC normalization). Note that MEREC uses an inverted normalization relative to the usual scheme:

$$n_{ij}^{x} = \begin{cases} \frac{\min_k x_{kj}}{x_{ij}}, & j \in B \\ \frac{x_{ij}}{\max_k x_{kj}}, & j \in NB \end{cases} \quad \ldots (1)$$

Step 3. Overall performance of each alternative (equal-weight logarithmic measure).

$$S_i = \ln\left(1 + \left(\frac{1}{n}\sum_j \left|ln\left(n_{ij}^x\right)\right|\right)\right) \quad \ldots (2)$$

Step 4. Performance with each criterion removed.

$$S'_{ij} = \ln\left(1 + \left(\frac{1}{n}\sum_{k,k\neq j} \left|ln(n_{ik}^x)\right|\right)\right) \quad \ldots (3)$$

Step 5. Removal effect and final weights.

$$E_j = \sum_i \left|S'_{ij} - S_i\right|, w_j = \frac{E_j}{\sum_k E_k} \quad \ldots (4)$$

The w_j obtained here are carried into the RAFSI criterion function.

2.7.2 Ranking by RAFSI

Step 6. Map the decision matrix into the criteria interval $[n_1, n_{2k}]$. For each criterion, define an ideal value a_{Ij} and an anti-ideal value a_{IIj} (For beneficial criteria, the ideal is the larger value; for non-beneficial, the smaller. Following the original method, the interval bounds are set so the ideal point is six times the anti-ideal: $n_1 = 1$ and $n_{2k} = 6$. Each element is then mapped linearly:

$$s_{ij} = \frac{n_{2k}-n_1}{a_{Ij}-a_{IIj}}\left(x_{ij} - a_{IIj}\right) + n_1 \quad \ldots (5)$$

(The same expression handles cost criteria automatically, since the slope becomes negative when $a_{Ij} < a_{IIj}$.)

Step 7. Form the normalized decision matrix using arithmetic and harmonic means of the interval.

$$A = \frac{n_1+n_{2k}}{2}, H = \frac{2}{\frac{1}{n_1}+\frac{1}{n_{2k}}} \quad \ldots (6)$$

$$\hat{s}_{ij} = \begin{cases} \frac{s_{ij}}{2A}, & j \in B \\ \frac{H}{2s_{ij}}, & j \in NB \end{cases} \quad \ldots (7)$$

Step 8. Compute the criterion function of each alternative (this is where the MEREC weights enter):

$$V(A_i) = \sum_{j=1}^{n} w_j \hat{s}_{ij} \quad \ldots (8)$$

Step 9. Rank the alternatives. Order alternatives in descending order $V(A_i)$. The highest value receives rank 1 and is selected for the subsequent work.

2.8 Testing of Void Content

Void content was evaluated using the hydrostatic weighing method, in which pore volume was estimated from the difference in sample mass before and after immersion. The percentage void content was calculated following ASTM D2734 using the difference between theoretical and experimentally measured composite densities (Thirupathi *et al.* 2025).

$$\mathrm{VV_p} = \frac{V_\mathrm{p}}{V} \times 100\% \quad \ldots (9)$$

2.9 Water Absorption

Water absorption was evaluated in accordance with ASTM D570 by measuring the percentage increase in specimen weight after immersion (Sajib *et al.* 2024). Composite samples measuring 10 mm × 10 mm were submerged in 250 mL of deionized water for 8 h to simulate moisture exposure. Following immersion, excess surface water was carefully eliminated by absorbent cotton cloth, and wet mass were recorded for water uptake calculations.

$$\mathrm{WA} = \frac{\text{Wet weight}-\text{Dry weight}}{\text{Dry weight}} \times 100\% \quad \ldots (10)$$

2.10 Moisture Content

Moisture of fabricated material was measured in accordance with ASTM D3790-17. Approximately 2.5 g of each specimen was placed in an aluminum dish and dried in a hot-air oven at 100 °C for 1 h. The samples were subsequently cooled, weighed, and returned to the oven for additional drying cycles until a constant mass was achieved. Moisture content was then calculated from the corresponding weight loss.

$$\text{Moisture Content} = \frac{\text{Final weight}-\text{Initial weight}}{\text{Initial weight}} \times 100 \ldots (11)$$

2.11 Antibacterial Analysis

Antibacterial activity was evaluated by the agar-disc diffusion method against *Escherichia coli* ATCC 25922 and *Bacillus subtilis* ATCC 6633 obtained from the Microbial Type Culture Collection. Bacterial suspensions were adjusted to 0.5 McFarland standard, corresponding to approximately 1.5×10^8 CFU mL^{-1}. Nutrient agar plates were inoculated uniformly with 100 µL of bacterial suspension. Sterilized circular composite specimens measuring 10 mm in diameter were placed on the inoculated agar. A gentamicin disc containing 10 µg served as the positive control, while the AgNP-free 25:75 coir/WPU composite served as the negative material control. The plates were incubated at 37 ± 1 °C for 24 h. Inhibition-zone diameters, including the specimen diameter, were measured in two perpendicular directions. Three independent plates were evaluated for each formulation, and the results were reported as mean ± standard deviation.

2.12 Experimental Reproducibility and Quality Control

Each composite formulation was prepared in three independent fabrication batches using freshly

prepared nanoparticle dispersions. Constituent masses were measured using an analytical balance with an accuracy of ±0.001 g. Mixing speed, mixing duration, mold dimensions, drying temperature, and relative humidity were maintained consistently for all batches. Composite thickness was measured at five locations using a digital micrometer, and specimens outside the target thickness of 2.0 ± 0.1 mm or containing visible cracks, incomplete edges, or large surface bubbles were excluded. Test specimens were randomly collected from different regions of each sheet and conditioned at 23 ± 2 °C and 50 ± 5% relative humidity for 48 h. Instruments were calibrated before testing, and blank, control, and replicate measurements were included where applicable. The coefficient of variation was maintained below 10% for replicate measurements.

3. RESULTS AND DISCUSSION

3.1 G-Ag and C-Ag Particle Analysis

Dynamic light scattering measurements were performed to evaluate the particle size distribution of synthesized Ag nanoparticles. Hydrodynamic diameters of chemically synthesized Ag (C-Ag) and green-synthesized Ag (G-Ag) nanoparticles were found to be 65–83 nm and 55 nm - 61 nm, respectively. As shown in Fig. 2, the relatively narrow distribution profiles indicate good particle size uniformity. The slightly larger size observed for G-Ag may be attributed to the influence of phytochemical constituents present in lemon peel extract, which act as capping and reducing agents during nanoparticle formation, leading to enhanced surface stabilization and moderate particle growth.

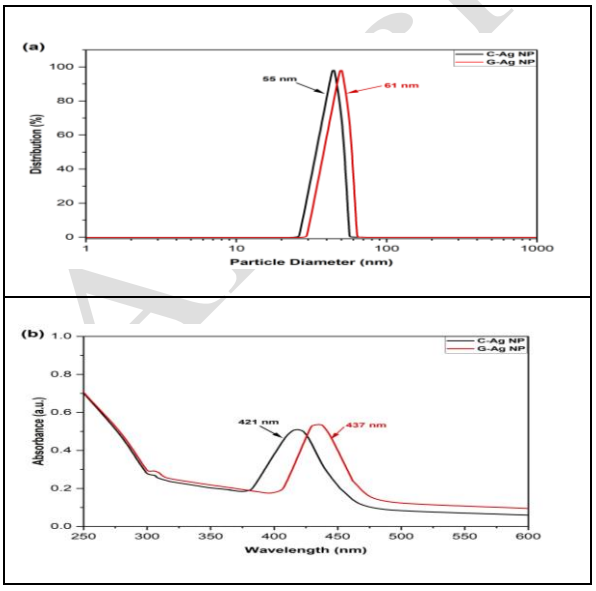

Fig. 2: (a) Size distribution with DLS of G-Ag nanoparticles and C-Ag nanoparticles and (b) UV spectrum of G-Ag nanoparticles and C-Ag nanoparticles

The UV–Visible spectra of G-Ag and C-Ag nanoparticles exhibited characteristic absorption maxima at 437 and 421 nm (Fig. 2), confirming successful formation of Ag nanoparticles. These absorption bands fall within the wavelength range commonly reported for silver nanostructures. The G-Ag sample displayed a slight shift toward a longer wavelength compared with C-Ag, which can be attributed to its comparatively larger particle size. This redshift behavior is consistent with the size-dependent optical properties of nanoparticles, where an increase in particle diameter results in absorption at higher wavelengths due to enhanced surface plasmon resonance effects.

3.2 Mechanical Properties

3.2.1 Optimization of Composite Composition

The control composites (A–G) are summarized at Table 1. The outcomes indicate TS and TM improved progressively with increasing coconut coir dust content, whereas elongation at break exhibited a declining trend. Composite A, consisting solely of water-borne polyurethane exhibited 3.2 ± 0.3 MPa tensile strength, 1.8 ± 0.2 MPa tensile modulus, and 118 ± 8% elongation at break and lower tensile strength and modulus. The incorporation of coconut coir dust enhanced stiffness and load-bearing capability, leading to gradual increases in strength and modulus up to composition F. Composite F exhibited the optimum mechanical performance with tensile strength, tensile modulus, and elongation values of 22.4 ± 1.0 MPa, 31.2 ± 1.1 MPa, and 31 ± 2%, respectively. A slight reduction in strength and modulus was observed for composite G, likely due to excessive filler loading, which may promote particle agglomeration and stress concentration sites within the composite matrix.

Table 1. Tensile response of the control composition

Sample	TS (MPa)	TM (MPa)	Elongation (%)
A	3.2 ± 0.3	L.8 ± 0.2	118 ± 8
B	5.4 ± 0.4	4.7 ± 0.4	96 ± 5
C	7.8 ± 0.5	8.6 ± 0.6	74 ± 4
D	10.6 ± 0.6	13.5 ± 0.8	58 ± 3
E	14.8 ± 0.8	19.4 ± 0.9	46 ± 2
F	22.4 ± 1.0	31.2 ± 1.1	31 ± 2
G	20.6 ± 0.9	27.8 ± 1.0	34 ± 2

One-way ANOVA confirmed statistically significant variations in TS, TM, and elongation at break among composites A–G, with p-values of 1.02×10^{-7},

8.69×10^{-10}, and 3.17×10^{-15}, respectively. Further evaluation using the Bonferroni post-hoc test revealed that composite F exhibited significantly superior mechanical performance compared with the remaining formulations at the adjusted significance level. Enhanced tensile strength indicates improved structural integrity and greater resistance to mechanical stresses during service.

Composite optimization was performed using the integrated MEREC–RAFSI approach based on the measured mechanical responses. Tensile strength and modulus were treated as beneficial criteria, whereas elongation at break was considered a non-beneficial criterion during the evaluation of composites A–G. The decision matrix was established using the experimentally obtained performance values and was shown in Table 2. Following the MEREC procedure, objective weights were assigned to each criterion according to their relative importance. To determine the optimum formulation considering multiple mechanical properties simultaneously, the MEREC–RAFSI multi-criteria decision-making approach was employed. The experimental results used as the decision matrix are presented in Table 2.

Table 2. Decision matrix

Sample	TS (MPa)	TM (MPa)	Elongation (%)
A	3.2	1.8	118
B	5.4	4.7	96
C	7.8	8.6	74
D	10.6	13.5	58
E	14.8	19.4	46
F	22.4	31.2	31
G	20.6	27.8	34

The MEREC method was applied to evaluate the relative importance of the selected criteria. The calculated criterion weights are presented in Table 3.

Table 3. MEREC criterion weights

Criterion	Weight
TS	0.0609
TM	0.5318
Elongation	0.4074

As shown in Table 3, tensile modulus (TM) received the highest weight of 0.5318, indicating that stiffness was the most influential parameter in the decision-making process. Elongation exhibited the second highest weight of 0.4074, demonstrating its significant contribution to material performance, whereas tensile strength (TS) received the lowest weight of 0.0609. These results suggest that the overall evaluation was predominantly governed by stiffness and deformation characteristics rather than strength alone.

Based on the criterion characteristics, the ideal and anti-ideal values required for the RAFSI method were determined and are presented in Table 4.

Table 4. Ideal and anti-ideal values

Criterion	Ideal	Anti-Ideal
TS	22.4	3.2
TM	31.2	1.8
Elongation	31	118

Using the MEREC-derived weights and the RAFSI methodology, the performance values and final rankings of all samples were calculated and are presented in Table 5.

Table 5. RAFSI performance values and ranking

Sample	RAFSI Value	Rank
A	0.4338	3
B	0.2813	7
C	0.2819	6
D	0.3311	5
E	0.4063	4
F	0.5662	1
G	0.5199	2

The RAFSI analysis identified Sample F as the optimum formulation with the highest performance score of 0.5662, followed by Sample G with a score of 0.5199. The superior ranking of Sample F can be attributed to its highest tensile strength (22.4 MPa), highest tensile modulus (31.2 MPa), and lowest elongation (31%), which closely correspond to the ideal solution. The high stiffness and strength of Sample F contributed significantly to its overall performance because tensile modulus was assigned the greatest weight in the MEREC analysis.

Sample G secured the second rank with a performance value of 0.5199 owing to its high tensile strength (20.6 MPa) and tensile modulus (27.8 MPa), together with a relatively low elongation of 34%. Although its properties were slightly inferior to those of Sample F, it still demonstrated excellent mechanical performance and remained close to the ideal condition.

Sample A achieved the third rank with a RAFSI score of 0.4338. Despite exhibiting the lowest tensile strength and modulus values, its high elongation contributed positively to the overall evaluation due to the considerable weight assigned to elongation. Samples E and D obtained intermediate rankings, indicating moderate mechanical performance. In contrast, Samples C and B occupied the lower ranks because of their comparatively lower stiffness and strength characteristics. Since tensile modulus was identified as the most influential criterion, deficiencies in stiffness substantially reduced their overall performance scores.

MEREC assigned the greatest importance to tensile modulus (0.5318), followed by elongation (0.4074) and tensile strength (0.0609). RAFSI ranked sample F first with a score of 0.5662, identifying the 25:75 coir/WPU formulation as the preferred composition for subsequent AgNP incorporation.

3.2.2 Mechanical comparison of G-Ag and C-Ag composites

Rather than considering each response independently, the results demonstrate a common concentration-dependent reinforcement mechanism: increasing AgNP content enhanced stiffness, tear resistance, hardness, and flexing endurance while reducing elongation, porosity, and moisture uptake. Tensile strength, modulus and elongation at break of G1–G4 and C1–C4 were illustrated at Figure 3. Both G-Ag and C-Ag reinforced composites exhibited comparable mechanical performance with tensile strength, modulus, and elongation values ranging from approximately 22.4–26.4 MPa, 31.2–42.2 MPa, and 27.4–31.0 %. One-way ANOVA indicating no statistically significant differences, produced p-values greater than 0.05, between the chemically synthesized and green synthesized Ag nanoparticle composites. Highest tensile strength and modulus was observed for G4 and C4 containing 5 wt.% Ag nanoparticles, while corresponding elongation values were the lowest. These findings suggest that, Ag nanoparticles function as effective nanofillers, contributing to improved reinforcement and structural compactness of the biocomposites. The simultaneous increase in strength and modulus and reduction in elongation indicate restricted polymer-chain mobility caused by AgNP reinforcement. However, the statistically comparable performance of G-Ag and C-Ag composites suggests that the synthesis route exerted less influence than nanoparticle loading.

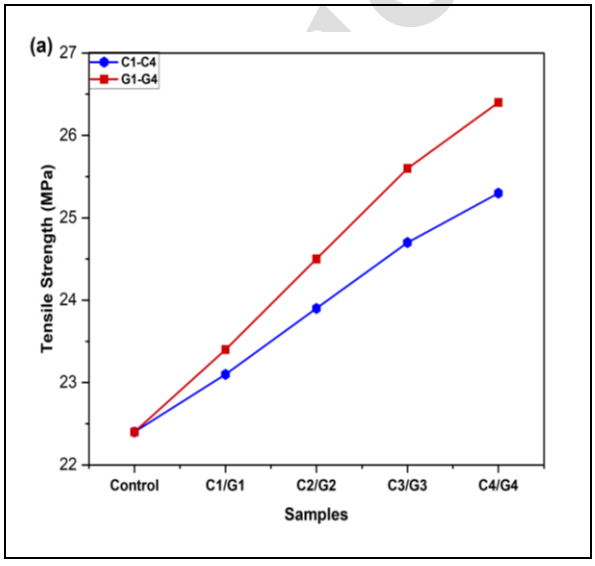

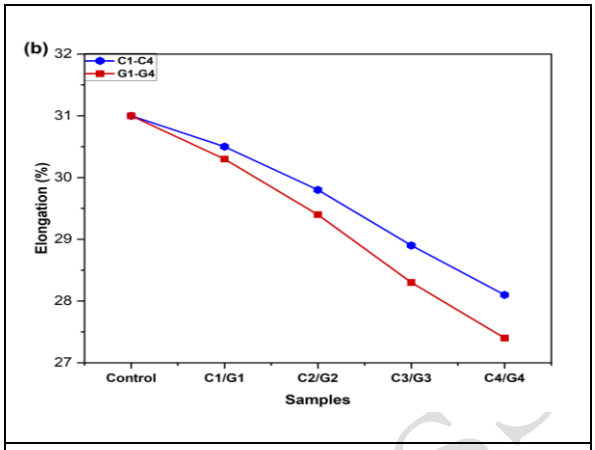

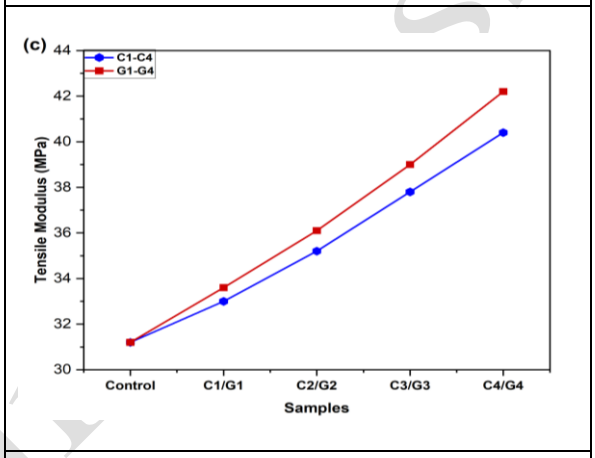

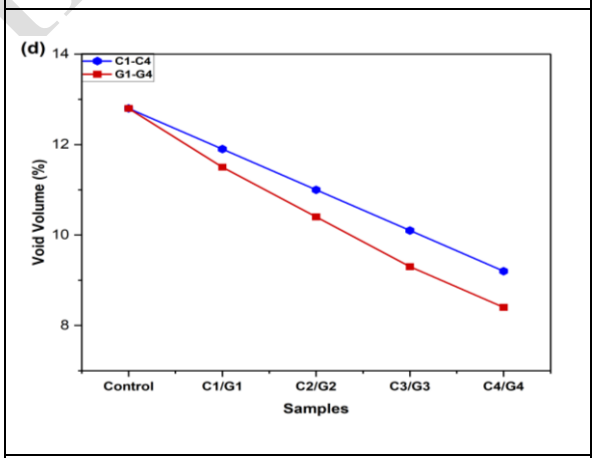

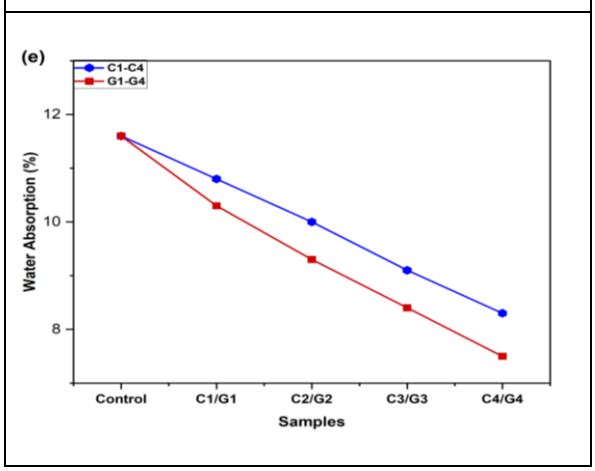

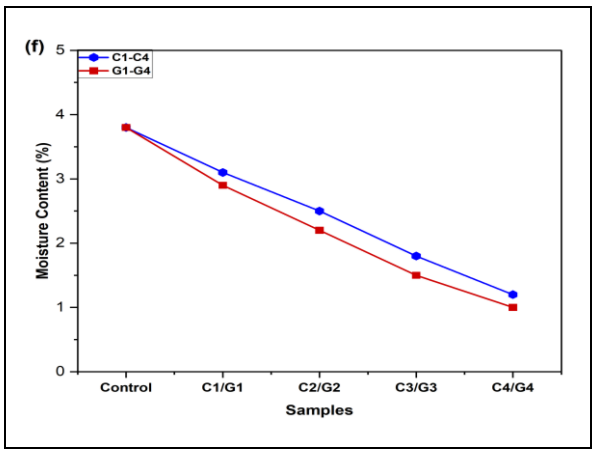

Fig. 3: Comparison of TS, TM, elongation percentage, water absorption, moisture content, and void volume among control, G-Ag, and C-Ag-composite

One-way ANOVA indicated no significant differences between corresponding G-Ag and C-Ag formulations ($p > 0.05$). Consequently, synthesis-route effects were interpreted cautiously, and observed numerical differences were not considered statistically conclusive.

3.3 Flexing Index

The flexural performance of fabricated composites was evaluated. Among the tested samples, G4 and C4 demonstrated the highest flexural endurance values of 9480 ± 26 and 9320 ± 25 cycles, respectively. The flexing index, calculated from the logarithmic value of the flexing cycles, was approximately 3.05 to 3.45 for all composites, including the control formulation. This value is considerably higher than the minimum requirement of 2.8, confirming excellent flexural resistance of the developed biocomposites.

Table 6. Tear strength, hardness flexing cycle, and flexing index of composites

Sample ID	Tear Strength (N/ mm)	Hardness	Flexing Cycle	Flexing Index
Control	812 ± 3	70.8 ± 0.2	8450 ± 25	3.05
C1	826 ± 3	71.4 ± 0.2	8680 ± 20	3.12
C2	841 ± 4	72.1 ± 0.3	8890 ± 22	3.20
C3	856 ± 4	73.0 ± 0.3	9110 ± 24	3.28
C4	871 ± 5	74.2 ± 0.4	9320 ± 25	3.36
G1	832 ± 3	71.8 ± 0.2	8760 ± 20	3.16
G2	849 ± 4	72.8 ± 0.3	8980 ± 22	3.25
G3	868 ± 4	74.0 ± 0.3	9240 ± 24	3.35
G4	885 ± 5	75.1 ± 0.4	9480 ± 26	3.45

3.4 Tear Strength

Tear resistance of the developed composites ranged from 812 to 885 N/mm, as presented in Table 6, indicating excellent resistance to tearing under localized loading conditions. The control composite exhibited the lowest tear strength (812 ± 3 N/mm), whereas the highest values were recorded for C4 and G4 with strengths of 871 ± 5 and 885 ± 5 N/mm. Statistical analysis using one-way ANOVA revealed no significant variation among the tested formulations. Similar to the trend observed for tensile modulus, tear resistance increased with increasing Ag nanoparticle content.

3.5 Hardness

Hardness of fabricated biocomposites were measured by digital durometer and was found to range from 71.4 ± 0.2 to 74.2 ± 0.4 for C-Ag composites and from 71.8 ± 0.2 to 75.1 ± 0.4 for G-Ag composites, as summarized in Table 6. The highest average hardness values were observed for C4 and G4. Statistical evaluation by one-way ANOVA indicated that, the differences among the formulations were not significant. The obtained hardness values were higher than those reported in comparable studies and demonstrated sufficient rigidity. The enhanced hardness may be attributed to the reinforcing effect of the incorporated Ag nanoparticles, which contributed to improved resistance against surface deformation.

3.6 Void Content Analysis

The biocomposites were fabricated through a hand-casting process without application of external compaction pressure, which led to the formation of internal voids. The void content of the control and Ag nanoparticle-reinforced composites was shown in Figure 3. The control composite exhibited the highest void fraction, approximately 12.8%, primarily due to air entrapment and non-uniform packing during fabrication. The incorporation of Ag nanoparticles reduced the void content, reaching about 8.4% and 9.2% for G4 and C4, respectively. The nanoscale particles likely occupied microvoid regions and improved matrix–filler packing efficiency. Notably, G4 and C4, which possessed the lowest void contents, also exhibited the highest tensile strengths, indicating a strong correlation between reduced porosity and enhanced mechanical performance.

3.7 Water Absorption Analysis

The water absorption behavior of the developed composites was evaluated, and the results are presented in Figure 3. The control composite exhibited the highest water uptake, approximately 11.5%, whereas C-Ag and G-Ag composites showed absorption values ranging from 8.3–10.7% and 7.5–10.2%, respectively. A noticeable reduction in water absorption was observed following Ag nanoparticle incorporation. This trend is consistent with the void content analysis, as lower porosity limits the availability of pathways for water penetration. Several researchers have examined water absorption; studies revealed that AgNP-treated natural fibers exhibited a significant reduction in moisture uptake compared to untreated fibers. This improvement is attributed to surface modification and increased roughness, which enhanced dimensional stability and limited water penetration into the fiber structure (da Silva Neto *et al.* 2026).

3.8 Moisture Content

The moisture content values measured at 4 h were 3.8%, 1.0%, and 1.2% for the control, G4, and C4, as shown in Figure 3. The incorporation of Ag nanoparticles significantly reduced the retained moisture content of composites compared with the control formulation.

3.9 Thermal Analysis

The TGA and DTG profiles of the control composite and the composites containing 5 wt.% Ag nanoparticles are shown in Fig. 4. An initial mass reduction of approximately 3.2–3.5% occurred near 140 °C for all formulations, which can be attributed to the removal of physically absorbed moisture and low-molecular-weight volatile compounds. At around 310 °C, the weight losses for the composite C4, G4, and control composites were 7.2%, 6.8%, and 8.8%, respectively. Further, thermal decomposition occurred near to 435 °C for C4, 440 °C for G4, and 428 °C for the control composite, where the Ag nanoparticle-reinforced composites exhibited approximately 69.5% and 68.2% mass loss, while the control composite showed a slightly higher loss of 70.0%. These degradation stages are clearly reflected in the corresponding DTG curves and are associated with the breakdown of polyurethane chains and lignocellulosic constituents. The G4 composite exhibited marginally lower weight loss than C4, indicating slightly improved thermal resistance. Furthermore, the residual masses at 600 °C were 14.8%, 15.6%, and 12.0% for the C4, G4, and control composites, respectively, confirming the enhanced thermal stability imparted by Ag nanoparticle incorporation. Overall, the addition of Ag nanoparticles enhanced the thermal stability of the developed biocomposites. In previous studies, thermogravimetric analysis (TGA) was used to evaluate the thermal stability of the gypsum–PVA–coconut fiber composites. The results indicated improved residue formation and enhanced decomposition resistance in the modified samples, confirming better thermal stability due to fiber treatment and PVA incorporation (Gonçalves *et al.* 2025).

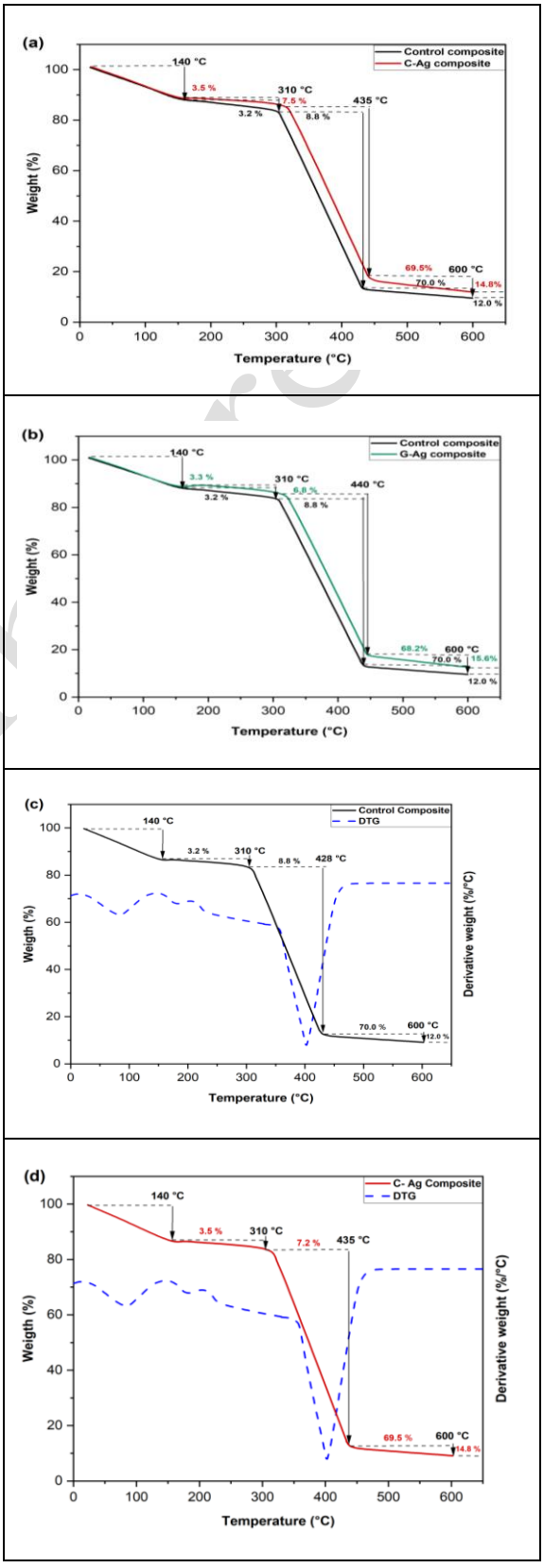

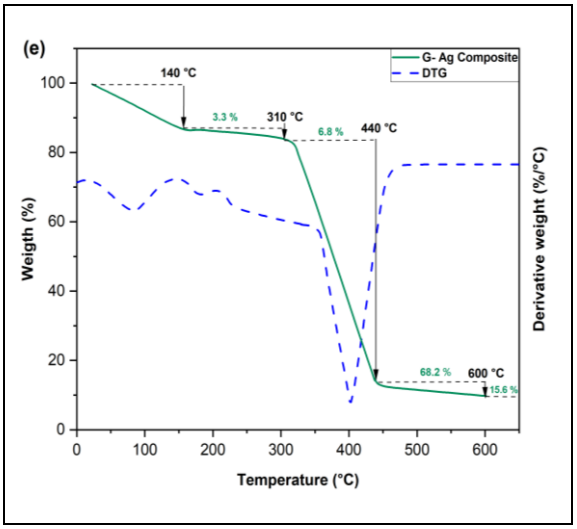

Fig. 4: Thermogravimetric analysis of (a) control, G-Ag composites (b) control, C-Ag-composite, DTG for (c) control, (d), GAg and (e) C-Ag

The principal degradation temperatures were approximately 428, 435, and 440 °C for the control, C4, and G4 composites, respectively. Their shift toward higher temperatures indicates delayed decomposition of the WPU–lignocellulosic structure after AgNP incorporation. Residues increased from 12.0% for the control to 14.8% and 15.6% for C4 and G4, respectively.

3.10 FTIR Spectroscopy

FTIR of G-Ag, C-Ag, coconut coir dust, water-borne polyurethane, and the corresponding composites were presented in Figure 5. Both G-Ag and C-Ag nanoparticles exhibited broad absorption near 3370 and 3348 cm^{-1}, attributed to O–H vibrations arising from adsorbed moisture and surface hydroxyl groups. Additional peaks in the lower wavenumber region are associated with Ag–O interactions and residual organic compounds originating from the synthesis process. The coconut coir dust spectrum displayed characteristic lignocellulosic bands, including O–H stretching (3335 cm^{-1}), C–H stretching (2918 cm^{-1}), C=O stretching (1605 cm^{-1}), aromatic skeletal vibrations (1512 cm^{-1}), and C–O/C–N related absorptions (1245 cm^{-1}). Water-borne polyurethane exhibited prominent peaks at 3340 cm^{-1}, 1604 cm^{-1}, 2925 cm^{-1} (C–H stretching), 1080 cm^{-1} (C–O bending), 1535 cm^{-1} (C–H deformation), and 1240 cm^{-1} (–CH_3 bending). Upon incorporation of Ag nanoparticles, the O–H absorption band shifted from 3340 cm^{-1} to 3318 cm^{-1} and 3330 cm^{-1} for G-Ag and C-Ag composites, indicating intermolecular interactions and hydrogen bonding between the composite constituents, thereby confirming improved interfacial compatibility within the matrix.

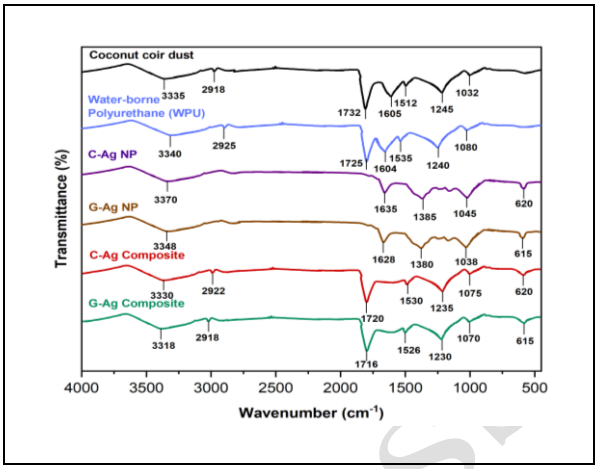

Fig. 5: FTIR of coconut coir dust, waterborne polyurethane, G-Ag NPs, C-Ag NPs, G-Ag composites and C-Ag composites

Minor shifts in the C–H stretching bands were observed for the Ag nanoparticle-reinforced composites. The C-Ag composite exhibited peaks at 2922 cm^{-1}, whereas the G-Ag composite displayed a dominant band near 2918 cm^{-1}. These spectral variations may be attributed to intermolecular interactions between the matrix constituents and Ag nanoparticles. A pronounced shift of the absorption band from 1605 cm^{-1} to approximately 1720–1716 cm^{-1} was also detected in both composites, suggesting modifications in the carbonyl-containing functional groups and enhanced interfacial interactions within the composite network. Additional bands appearing near 620 and 615 cm^{-1} in G-Ag and C-Ag composites are associated with Ag-related vibrational features and nanoparticle incorporation into the matrix structure. Several researchers have reported that the FTIR analysis confirmed the presence of characteristic cellulose functional groups such as O–H, C–H, and C–O–C stretching vibrations, indicating successful formation of bacterial cellulose. The spectra exhibited slight shifts in peak positions, suggesting interactions between additives and cellulose chains (Agustina *et al.* 2025). The observed peak shifts and band modifications collectively indicate strong interactions among coconut coir dust, water-borne polyurethane, and Ag nanoparticles, which are further supported by the improved mechanical properties and FESEM observations. The O–H shift from 3340 cm^{-1} to 3318–3330 cm^{-1} suggests altered hydrogen-bonding environments among coir, WPU, and AgNP surfaces. Changes around 1720–1716 cm^{-1} indicate modification of carbonyl interactions rather than formation of new covalent bonds. These interactions may restrict chain mobility and contribute to the observed stiffness increase.

3.11 XRD Analysis

Crystalline characteristics of synthesized Ag nanoparticles were examined through XRD analysis. Distinct diffraction peaks corresponding to C-Ag and G-Ag nanoparticles were observed at 38.1°, 44.3°, 64.4°, and 77.4° (2θ), confirming the formation of crystalline Ag nanostructures. The intense and sharp diffraction peaks show good crystallinity of the synthesized particles. Based on the Debye–Scherrer equation, average crystallite sizes were estimated as 21.0 and 20.84 nm for C-Ag and G-Ag nanoparticles, respectively. The calculated crystallinity values were approximately 91.0% for C-Ag and 91.2% for G-Ag, demonstrating a highly ordered crystal structure. The peaks at 38.1°, 44.3°, 64.4°, and 77.4° were assigned to the (111), (200), (220), and (311) planes of face-centered-cubic silver, respectively, consistent with ICDD PDF No. 04-0783. Crystallinity was calculated as the ratio of integrated crystalline-peak area to total diffracted area after baseline correction.

In contrast, the XRD patterns of the fabricated composites exhibited broader diffraction bands, characteristic of predominantly amorphous polymeric matrices. Nevertheless, the Ag nanoparticle-containing composites displayed several low-intensity crystalline peaks associated with the incorporated nanoparticles, confirming their successful integration within the matrix. Broad diffraction maxima centered around 22–24° (2θ) were observed for the control, G-Ag, and C-Ag composites and are attributed to the semi-crystalline nature of the lignocellulosic coir component. ;'Crystallinity indices of control, G-Ag, and C-Ag composites were determined as 23%, 36%, and 34%, respectively. The increase in crystallinity following Ag nanoparticle incorporation further supports the reinforcing effect of the nanoparticles within the composite structure. Previous research has demonstrated that XRD analysis was used to determine the crystalline structure and phase composition of the PVA-based composite. It provides insights into crystallinity, crystallite size, and structural modifications induced by wheat husk, coconut fibers, and aloe vera incorporation. The results also confirm changes in lattice arrangement, molecular ordering, and the overall structural stability of the developed biodegradable (Singh *et al.* 2023).

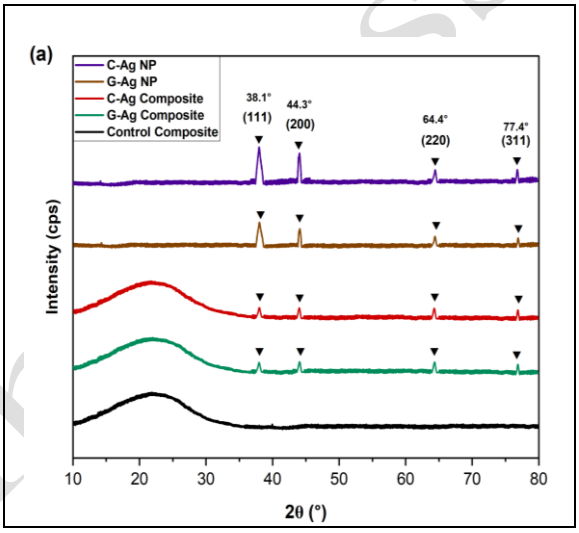

Fig. 6: XRD for G-Ag NPs, C-Ag NPs, C-Ag composites, G-Ag composites and control

Table 7. Crystallite size of G-Ag and C-Ag nanoparticles

C-Ag Nanoparticles				G-Ag Nanoparticles			
Peak Position	FWHM	Crystallite Size, D	Average D	Peak Position	Crystallite Size, D	FWHM	Average D
38.1	0.39	22.8	21.0	38.1	0.40	21.9	20.84
44.3	0.42	21.7		44.3	0.43	21.2	
64.4	0.48	20.4		64.4	0.49	20.1	
77.4	0.52	19.1		77.4	0.53	18.9	

3.12 FESEM and Elemental Analysis

FESEM micrographs was employed to examine morphology and particle size of synthesized Ag nanoparticles. Nanoparticles exhibited predominantly spherical morphology with average diameters of approximately 66 nm for G-Ag and 61 nm for C-Ag, which is consistent with the nanoscale dimensions obtained from DLS measurements. DLS produced hydrodynamic diameters of 55 and 61 nm for C-Ag and G-Ag, whereas FESEM showed physical particle sizes of approximately 61 and 66 nm, respectively. These small differences arise from solvation, particle aggregation, image-sampling variation, and the different measurement principles. XRD yielded smaller crystallite sizes of 21.0 and 20.84 nm because individual particles may contain multiple crystalline domains. Chemical synthesis provided rapid reduction and controlled processing but required $NaBH_4$ and generated chemical residues. Green synthesis reduced hazardous-reagent consumption and

produced slightly better antibacterial performance, although phytochemical variability resulted in a marginally larger particle size. Thus, green synthesis offers greater environmental advantages, whereas chemical synthesis provides better compositional control.

Surface and cross-sectional morphologies of the composites were also investigated using FESEM, as illustrated in Fig. 7. The micrographs revealed the presence of irregularly distributed pores, which can be attributed to the hand-casting process performed without external compaction. Cross-sectional images demonstrated the fibrous structure of coconut coir dust embedded within the water-borne polyurethane matrix, indicating satisfactory interfacial bonding. Ag nanoparticles were visibly distributed throughout the composite matrix, with minor localized agglomeration observed in certain regions. FESEM images indicated the presence of AgNP-like features within the matrix, with minor localized agglomeration. Because elemental mapping was not performed, the images provide qualitative rather than conclusive evidence of nanoparticle dispersion and interfacial bonding. Previous studies have reported that, the FESEM analysis revealed that the silt-retting process effectively removed surface impurities, pectin, and other non-cellulosic substances from the coconut husk fibers. The treated fibers exhibited a cleaner, rougher, and more distinct fibrillar surface morphology, which is beneficial for improved fiber–matrix adhesion in composite applications (Ru *et al.* 2025).

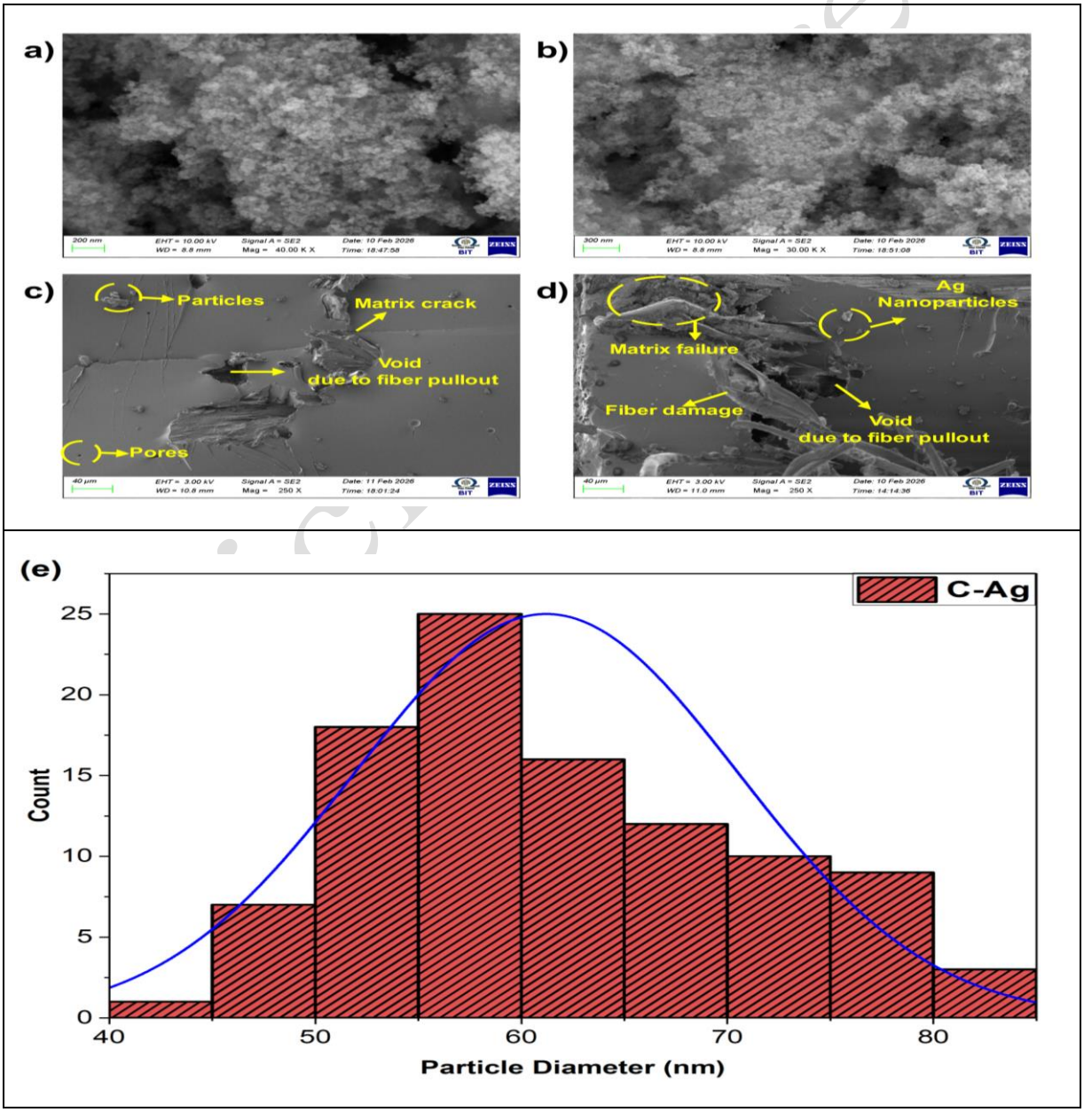

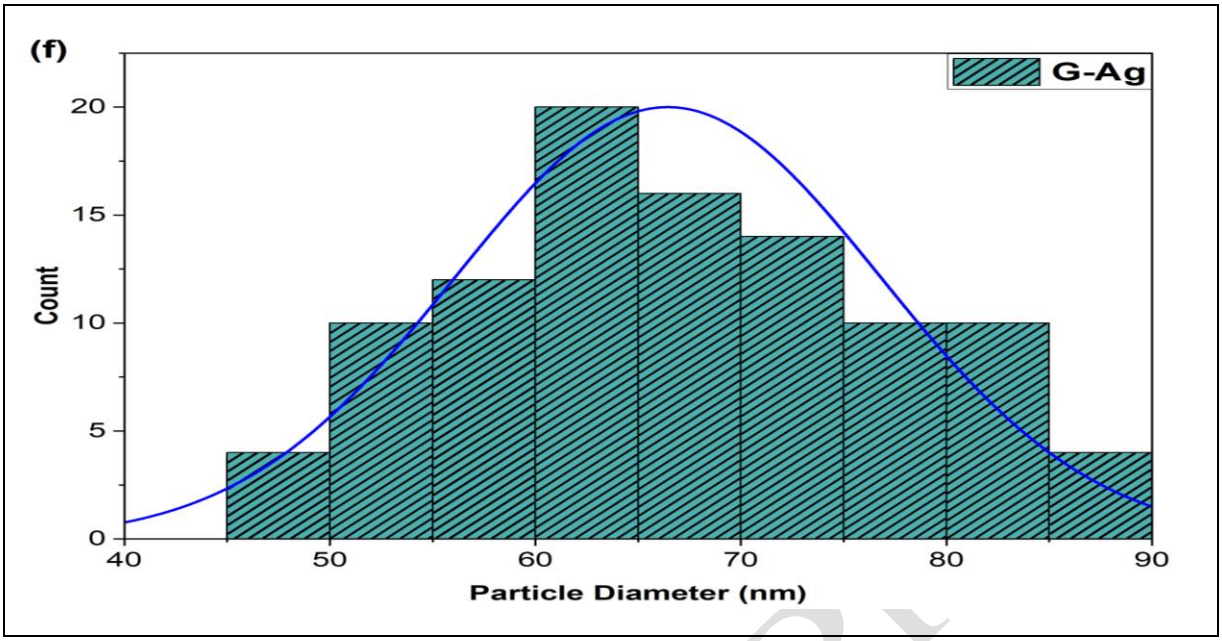

Fig. 7: FESEM of (a) G-Ag, (b) C-Ag, (c), composite cross-section, and (d) composite surface; histogram of FESEM for (e) GAg and (f) C-Ag nanoparticle size distribution

3.13 Antibacterial Activity

Ag nanoparticle-incorporated composites exhibited pronounced antibacterial activity against both Gram-negative and Gram-positive bacteria, Escherichia coli and *Bacillus subtilis*. The inhibition zone increased progressively with increasing Ag nanoparticle concentration, as illustrated in Figure 8. This behavior can be attributed to enhanced release of Ag^{+} ions and the increased interaction of nanoparticles with bacterial cell membranes, resulting in more effective suppression of microbial growth. The composites demonstrated higher antibacterial effectiveness against *B. subtilis* than against *E. coli*, with inhibition zones reaching approximately 15.3 mm and 14.2 mm, respectively. The antibacterial performance improved by approximately 33% and 42% against *B. subtilis* and by approximately 31% and 30% against *E. coli* for G-Ag and C-Ag composites, respectively, when the nanoparticle loading increased from 1.25% to 5 wt.%. At equivalent Ag concentrations, the G-Ag composites displayed slightly superior antimicrobial activity compared with the C-Ag formulations. This enhancement may be associated with residual phytochemicals from lemon peel extract, including phenolic and flavonoid compounds, which can adsorb on the nanoparticle surface and contribute synergistically to the antibacterial mechanism. In previous studies, lemon peel extract-loaded films exhibited effective antibacterial activity against both *Escherichia coli* and *Staphylococcus aureus*, demonstrating broad-spectrum antimicrobial performance. The incorporation of lemon peel extract enhanced bacterial growth inhibition while maintaining desirable material properties (Mortazavi *et al.* 2023).

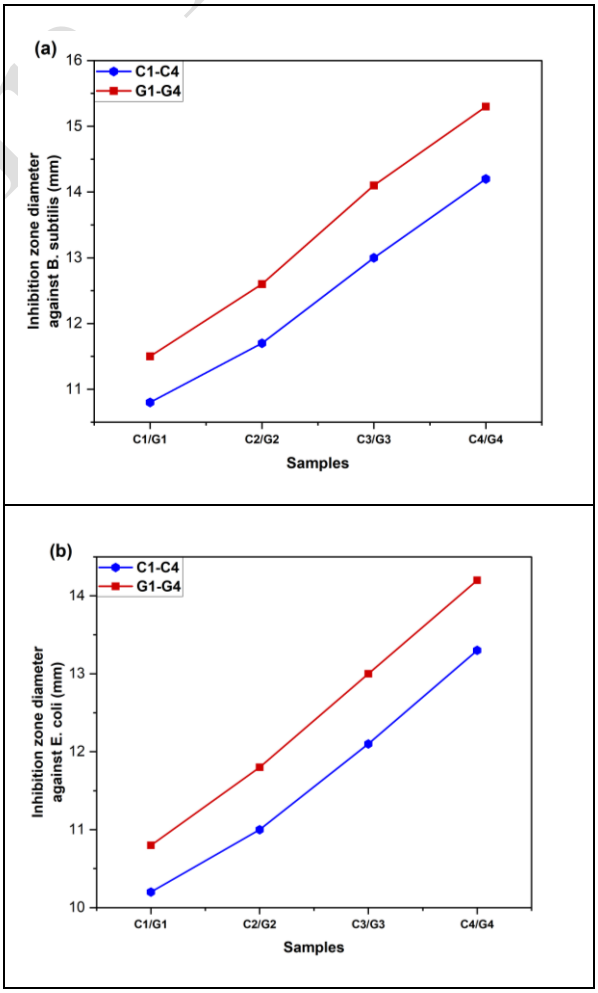

Fig. 8: Antibacterial zone at (a) *B. subtilis* and (b) *E. coli*

The results demonstrate an interconnected structure–property relationship. AgNP incorporation reduced void content from 12.8% to 8.4–9.2%, thereby limiting water penetration and retained moisture. Improved matrix compactness corresponded with higher tensile strength, modulus, tear resistance, hardness, and thermal residue. Increasing AgNP availability also enhanced antibacterial activity through greater Ag^+ release and bacterial contact. G4 therefore provided the best combined mechanical, moisture-resistant, thermal, and antibacterial performance.

4. CONCLUSION

Ag nanoparticles synthesized through green and chemical routes were successfully incorporated into coconut coir dust/WPU biocomposites, as supported by UV–Visible, XRD, FTIR, and FESEM analyses. G-Ag nanoparticles showed a larger hydrodynamic particle size (61 nm) and a marginally smaller crystallite size (20.84 nm) compared with C-Ag nanoparticles (91.0%, 55 nm, and 21.0 nm, respectively). UV–Visible, XRD, and FTIR analyses verified the successful synthesis of Ag nanoparticles and their incorporation within the composite system. FESEM micrographs revealed nanosized particles distributed throughout the matrix with minor agglomeration and confirmed satisfactory dispersion of Ag nanoparticles within the developed biocomposites. Based on the MEREC–RAFSI optimization approach, the composite containing 25 wt.% coconut coir dust and 75 wt.% water-borne polyurethane was identified as the optimum control formulation. The developed Ag nanoparticle-reinforced composites exhibited mechanical properties exceeding the minimum requirements for footwear insoles, together with acceptable moisture absorption and moisture retention characteristics. Furthermore, tear resistance, flexing durability, and hardness values satisfied relevant performance criteria. Among the developed formulations, G4 demonstrated superior antibacterial activity, exhibiting approximately 8% and 7% greater inhibition against *Bacillus subtilis* and *Escherichia coli*, respectively, than C4. Overall, this study demonstrates an effective route for converting coconut coir dust into value-added antibacterial biocomposites through the incorporation of green-synthesized Ag nanoparticles. Overall, the study provides a sustainable materials-development strategy for converting coconut coir waste into value-added multifunctional antibacterial biocomposites.

FUNDING

This research received no specific grant from any funding agency in the public, commercial, or not-for-profit sectors.

CONFLICTS OF INTEREST

The authors declare that there is no conflict of interest.

REFERENCES

Agustina, W., Gamonpilas, C. and Boontawan, A., Effect of additives on bacterial cellulose yield and properties in Thai red tea Kombucha fermentation, *Int. J. Bio. Macromol.*, 334, 149143(2025). https://doi.org/10.1016/j.ijbiomac.2025.149143

Arumugam, C., Arumugam, S. and Muthusamy, S., Mechanical, thermal and morphological properties of unsaturated polyester/chemically treated woven kenaf fiber/AgNPs@PVA hybrid nanobiocomposites for automotive applications, *J. Mater. Res. Technol.*, 9(6), 15298–15312(2020). https://doi.org/10.1016/j.jmrt.2020.10.084

Balasubramanian, B., Balasubramanian Karthekeyan, P., Noor Mohamed, M. R., Krishnankutty, P., Amarnath, M. K., Pandiarajan, N., Mavinkere Rangappa, S. and Siengchin, S., PVA/CSP/AgNPs hybrid biocomposite films: Optimization of process constraints using Taguchi-based grey relational analysis and functional property evaluation, *J. Thermoplast. Compos. Mater.*, 39(4), 1637–1666(2026). https://doi.org/10.1177/08927057251368876

Blessymol. B. V. Kalaiselvi, V. Yasotha. P. Gopi. S, Comparative Study of Chemically and Green Synthesized Titanium Dioxide Nanoparticles using Leucas aspera Leaf Extract, *J. Environ. Nanotechnol.,* 12 (3) 10-13 (2023). https://doi.org/10.13074/jent.2023.09.233471

Boncooğlu, R. Y., Bursali, F., Aytar, M. and Celik, A., Green Synthesis of Silver Nanoparticles From Three Endemic Plants in Türkiye: Antioxidant, Antimicrobial, and Larvicidal Activities, *Chem. Select*, 11(17), e05719(2026). https://doi.org/10.1002/slct.202505719

Camillo, M. D. O., Gonçalves, B. M. M., Candido, V. S., Dias, L. D. C., Moulin, J. C., Monteiro, S. N. and Oliveira, M. P., Assessment of Hydrothermal Treatment Effects on Coir Fibers for Incorporation into Polyurethane Matrix Biocomposites Derived from Castor Oil, *Polym.*, 15(23), 4614(2023). https://doi.org/10.3390/polym15234614

da Silva Neto, G. A., Guimarães, C. C., Mania, E., Kamida, H. M., da Silva, M. V. S., Toledo Filho, R. D. and Lima, P. R. L., Impact of silver nanoparticle impregnation on natural fiber properties and fiber–cement interactions, *J. Build. Pathol. Rehabilitat.*, 11(2), 145(2026). https://doi.org/10.1007/s41024-026-00815-9

Dayana, B. M., Venkatesan, R., Joseph Prakash, J. T., Saravanan, P., Nivetha, M. S., Murali, A., Vetcher, A. A., Settu, M. and Kim, S. C., Biosynthesis of silver nanoparticles via Melaleuca alternifolia leaf extract for antibacterial, antifungal, antioxidant and anticancer activity, *Sci. Rep.*, 16(1), 2574(2026). https://doi.org/10.1038/s41598-025-32191-8

Debnath, R., Das, B. K., Paul, S., Bhattacharjee, S. and De, U. C., Green Synthesis of Silver Nanoparticles Using Spermacoce alata Leaf Extract with Enhanced Antibacterial, Antioxidant, and Catalytic Performance, *Chem. Nano. Mat.*, 12(3), 0581(2026). https://doi.org/10.1002/cnma.202500581

Deleanu, I. M., Busuioc, C., Deleanu, M., Stoica-Guzun, A., Rotaru, M., Ștefan, V. A. and Isopencu, G., Antimicrobial Carboxymethyl Cellulose-Bacterial Cellulose Composites Loaded with Green Synthesized ZnO and Ag Nanoparticles for Food Packaging, *Int. J. Mol. Sci.*, 25(23), 12890(2024). https://doi.org/10.3390/ijms252312890

Ertekin, Ö., Evaluation of poly(lactic acid) films incorporated with lemon peel extract oil for food packaging materials, *CYTA – J. Food*, 23(1), 2516483(2025). https://doi.org/10.1080/19476337.2025.2516483

Gonçalves, S. C., da Silva Junior, M. F., Souza, M. T., Júnior, N. S. D. A. and Ribeiro, D. V., Physicomechanical Properties of Recycled Gypsum Composites with Polyvinyl Acetate Emulsion and Treated Short Green Coconut Fibers, *Build.*, 15(19), 3490 (2025). https://doi.org/10.3390/buildings15193490

Guerrero, E. G., Posada, P. A., Ríos-Rojas, J. F., Rincón, J., Amaya, J., Perez, D. L. and Rozo, A. P., Surface and interface engineering of biosynthesized AgNP–silica sol–gel coatings for simultaneous bacterial inhibition and corrosion protection, *Surf. Interf.*, 86, 108746(2026). https://doi.org/10.1016/j.surfin.2026.108746

Gupta, R. K., Saravanan, V., Manikandan, K., Shalom, N., Arun kumar, K. and Mayakannan, S., Fatigue, impact, and mechanical behavior of tamarind cellulose reinforced birch/Khusha grass fiber hybrid bio composites, *Interact.*, 247(1), 104(2026). https://doi.org/10.1007/s10751-026-02445-6

Hassan, D., Sani, A., Chanihoon, G. Q., Antonio Pérez, A., Ehsan, M. and Torres Huerta, A. L., Environmentally Sustainable and Green Polymeric Method for Chitosan (CH) Film Synthesis Using Natural Acids and Impact of Zinc Ferrite Nanoparticles (NPs) on Water Solubility (WS) and Physical Properties, *Polym.*, 16(24), 3466(2024). https://doi.org/10.3390/polym16243466

Jumaidin, R., Gazari, A. S., Kamaruddin, Z. H., Kamaruddin, Z. H., Zakaria, N. H., Kudus, S. I. A., Yob, M. S., Munir, F. A. and Keshavarz, M., Mechanical Properties of Thermoplastic Cassava Starch/ Coconut Fibre Composites: Effect of Fibre Size, *Pertanika J. Sci. Technol.*, 32(S2), 91–113(2024). https://doi.org/10.47836/PJST.32.S2.07

Kamalesan, M., Raja, M., Neelamegam, R., Kamble, S. S., Shyu, D. J. H. and Nagarajan, K., Eco-Friendly Synthesis and Characterization of Calotropis gigantea-Derived Silver Nanoparticles for Combating Antibiotic-Resistant *Helicobacter pylori* and Gastric Cancer Cells, *Pharma.*, 19(3), 358(2026). https://doi.org/10.3390/ph19030358

Kannan, G. and Thangaraju, R., Evaluation of Tensile, Flexural and Thermal Characteristics on Agro-Waste Based Polymer Composites Reinforced with Banana Fiber/Coconut Shell Filler, *J. Nat. Fib.*, 20(1), 2154630 (2023). https://doi.org/10.1080/15440478.2022.2154630

Krishnasamy, B., Gladston, A. K., Sekar, C. B. and Selvaraju, M., Investigation on the thermal, mechanical, and morphological characterization of peepal fiber-reinforced epoxy composites enhanced with micro-particulate ziziphus mauritiana seed powder, *Revista Materia*, 31, e20250643(2026). https://doi.org/10.1590/1517-7076-RMAT-2025-0643

Kularia, G., Sharma, Y., Verma, A., Bhatia, R., Anand, V. and Heera, P., Comparative evaluation of green synthesized silver nanoparticles using Psidium guajava and Azadirachta indica leaf extracts for photocatalytic and antibacterial applications, *Next Mater.*, 12, 102283(2026). https://doi.org/10.1016/j.nxmate.2026.102283

Lemeitaron, N. P., Shigwenya, M. E., Munuhe, L. N., Makhanu, S. D. and Kinyanjui, K. P., Green synthesis of silver nanoparticles via aqueous extracts of *Prunus africana* and their antimicrobial activities, *South African J. Chem. Eng.*, 57, 100883(2026). https://doi.org/10.1016/j.sajce.2026.100883

Meniche, A., Fatmi, S., Chibani, N., Ihamouchen, C. and Skiba, M., Valorization of tomato processing waste for the green synthesis of silver nanoparticles and evaluation of their effects on the properties of sodium alginate matrices, *Polym. Bulletin*, 83(6), 317 (2026). https://doi.org/10.1007/s00289-026-06373-x

Mortazavi, M. F. A., Khoshkalampour, A., Mortazavi Moghadam, F. A., PourvatanDoust, S., Naeijian, F. and Ghorbani, M., Preparation and physicochemical evaluation of casein/basil seed gum film integrated with guar gum/gelatin based nanogel containing lemon peel essential oil for active food packaging application, *Int. J. Bio. Macromol.*, 224, 786–796(2023). https://doi.org/10.1016/j.ijbiomac.2022.10.166

Osorio, C. K. F., Omisol, C. J. M., Asequia, D. M. A., Aguinid, B. J. M., Erjeno, D. J. D., Tejas, K. J. G. D., Dingcong, R. G., Tomon, T. R. B., Hisona, R. M. R., Etom, A. E., Triana, A. P. G., Dumancas, G. G., Alguno, A. C., Zoleta, J. B., Malaluan, R. M. and Lubguban, A. A., Synthesis of green-based carbon-doped nanosilica for enhanced mechanical properties of coconut oil-based rigid polyurethane foam, *RSC Appl. Polym.*, 3(5), 1356–1365(2025). https://doi.org/10.1039/d5lp00161g

Pereira, T. G. T., Faria, D. L., Silva, D. W., de Sousa Arantes, L., Soriano, J., Batista, F. G., Von Pinho Hostalácio, J. M., Mendes, L. M. and Tonoli, G. H. D., Improved performance of coconut fiber and quartzite waste cement composites using accelerated carbonation, *Environ. Sci. Pollut. Res.*, 32(18), 11562–11580(2025). https://doi.org/10.1007/s11356-025-36349-9

Ramkumar, T., Hariharan, K., Selvakumar, M. and Jayaraj, M., Effect of Various Surface Modifications on Characterization of New Natural Cellulosic Fiber from Coconut Tree Secondary Flower Leaf Stalk Fiber (CSF), *J. Nat. Fib.*, 19(16), 13362–13375(2022). https://doi.org/10.1080/15440478.2022.2091715

Ru, S., Zhang, Y., Yang, R., Zhang, X. and Yang, S., Characterization based on silt retting method for extracting fibers from waste coconut husks, *Indus. Crops Prod.*, 237, 122278(2025). https://doi.org/10.1016/j.indcrop.2025.122278

Ru, S., Zhao, C. and Yang, S., Multi-Objective Optimization and Analysis of Mechanical Properties of Coir Fiber from Coconut Forest Waste, *Forests*, 13(12), 2033(2022). https://doi.org/10.3390/f13122033

Sajib, M. A. R., Islam, M. S., Arifuzzaman, M. and Shoily, S. K., Effect of wood varnish coating on the water absorption and mechanical properties of jute fiber reinforced epoxy composites, *Heliyon*, 10(18), e37433 (2024). https://doi.org/10.1016/j.heliyon.2024.e37433

Singh, S. K., Srivastava, A. and Asthana, N., Development and Characterization of PVA based Green Nanocomposite Membrane for Next Generation Sustainable Food Packaging Applications, *Ind. J. Eng. Mater. Sci.*, 30(3), 474–483(2023). https://doi.org/10.56042/ijems.v30i3.3651

Sivaranjani Varadharajan, Parthiban Pandian, Antioxidant, Antimicrobial, and Potential Biomedical Applications of Green Synthesized Silver Nanoparticles Using Aloe barbadensis Root, *J. Environ. Nanotechnol.,* 14 (1) 97-103 (2025) https://doi.org/10.13074/jent.2025.03.2511226

Subbarao, E., Sharma, D., Singh, P., Gupta, R. K., Gayathri, B. and Mayakannan, S., Influence of B_4C and TiO_2 fillers on mechanical and tribological performance of Canna indica/Curaua fiber reinforced hybrid composites with ANN prediction, *Interact.*, 247(1), 148(2026). https://doi.org/10.1007/s10751-026-02511-z

Tavukcuoglu, O., Ciftci, F., Evcimen Duygulu, N., Coban, M. E., Misirli, D. and Elmastas, M., Silver nanoparticles from Arbutus unedo extract: Green synthesis, antibacterial activity, and TMPRSS2 enzyme inhibition, *Food Biosci.*, 80, 109011(2026). https://doi.org/10.1016/j.fbio.2026.109011

Thirupathi, S., Gopalan, V. and Mallichetty, E., Investigation of void content in Borassus flabellifer fiber/epoxy bio-nanocomposite using hyperparameter tuned ANN and response surface methodology optimization, *Sci. Rep.*, 15(1), 22757(2025). https://doi.org/10.1038/s41598-025-06740-0